

## Full Length Article

## A detailed tire tread friction model considering dynamic friction states

Meng Zhang<sup>\*</sup>, Hans-Joachim Unrau, Martin Gießler, Frank Gauterin*Institute of Vehicle System Technology, Karlsruhe Institute of Technology (KIT), Rintheimer Querallee 2, Karlsruhe, 76131, Germany*

## ARTICLE INFO

## Keywords:

Tire tread friction modeling  
 Dynamic friction states  
 Viscoelastic effect  
 Two-dimensional contact patch

## ABSTRACT

Characterizing tire tread friction behavior across various driving scenarios remains challenging due to complex rubber properties. Addressing this, we present a viscoelastic model enhanced with detailed dynamic friction states of the tread. Specifically, this novel model comprehensively accounts for a two-dimensional contact patch and key rubber features such as viscoelasticity, adaptable elasticity, and the speed/load dependency of the coefficient of friction. Experiments with solid rubber wheels validate the model's accuracy in capturing tread rubber friction performance under diverse loads and speeds. Finally, the comparison with other models underscores the advancement of the proposed model and provides valuable insights for sophisticated tire tread friction modeling. This research forms the base for exploring friction-related tire wear and particle emissions.

## 1. Introduction

The tire significantly influences vehicle performance, including safety, maneuverability, and comfort. Precise modeling of the tire friction is essential not only to improve the efficiency of tire and vehicle development but also to leverage the potential capability to optimize overall vehicle performance.

The relevant work about tire modeling can date back to the early 20th century [1]. In 1941, in order to address the shimmy phenomenon in aircraft landing gear systems, von Schlieppe [2] proposed a string tire model. Around the same time, Fromm [3,4] developed an initial brush-type model aimed at evaluating tire cornering properties. In 1969, Dugoff [5] proposed a tire model based on the brush theory, which introduced an adjustment factor to regulate longitudinal and lateral tire forces. The Dugoff model considered the coefficient of friction (CoF) as a linearly decreasing function over sliding speed. Later, Gim [6] adopted a similar friction law and proposed the UA-GIM tire model for cambered tires. The UA-GIM model utilized a parabolic contact pressure distribution and provided insights into the local friction force in the contact patch, in addition to the overall tire grip performance.

Benefiting from advancements in computing power, the viscoelastic effect of rubber has received increasing attention. Building upon Dahl's research [7,8], C. Canudas et al. [9,10] proposed the LuGre friction model by considering the speed dependence of the steady state friction force. Although the LuGre model was originally developed to study friction in control systems, it has since been widely applied to tire friction [11–15]. However, since the inertia of tread elements is not taken into account, the sliding speed of rubber is determined in a

manner that straightly refers to the ratio between the rubber elastic force and the friction force. By integrating the inertia of tread elements into a brush model, Mavros [16] numerically calculated the sliding speed of rubber elements based on the dynamic friction states of the elements. Nevertheless, the resulting friction force depicted a considerable deviation from the reference value, attributable to the under-consideration of the rubber friction law, as explained by the author. Later, Simoni et al. [17] and Hieu et al. [18] proposed an extended LuGre model that incorporates dwell time as an internal state variable, thereby capturing the variation of friction with time when the relative velocity of the two surfaces is held constant. However, this approach is too complex and difficult to use for evaluating tire tread friction. Shao et al. [19] studied rubber friction using a single Generalized Maxwell element, and explored the dynamic friction behavior of rubber samples during sliding. This approach reveals the possibility of estimating the tangential shear stress distribution in the contact patch, but the feasibility of extending the model to assess overall tire force performance was not examined.

On the other hand, researchers also give insights into refining the approximation of a more realistic contact patch and associated contact pressure distribution. Sakai [20–23] constructed a brush-type tire model that used multiple individual tread ribs to represent the contact patch. Each rib possessed an independent contact pressure distribution that approximated the actual contact pressure through piecewise functions. Davari [24] integrated Generalized Maxwell elements and introduced an Extended Brush Model (EBM) with a two-dimensional (2D) contact patch. In EBM, the tire's cross-sectional shape was considered as an arc, and the contact pressure distribution was determined

<sup>\*</sup> Corresponding author.

E-mail address: [meng.zhang@kit.edu](mailto:meng.zhang@kit.edu) (M. Zhang).

according to the tire's vertical compression. Sarkisov [25] built a brush-type tire model incorporating a 2D contact patch to investigate the tire carcass deflection behavior under the tire side force in more detail. In parallel, Riehm et al. [26] devised a tire model using a 2D contact patch and authentic contact pressure to improve the evaluation of rubber sample friction characteristics on an indoor test rig. Later, they further extended this 2D modeling method to encompass full-size tire simulation [27], in which the shape of the contact patch and the contact pressure distribution of each tire rib were considered. However, these two models did not take into account the force balance of rubber elements in determining their friction states during sliding.

Despite the progress made in evaluating tire friction behaviors, certain aspects still require refinement [20,28–30]. For instance, the change of rubber properties and the resulting rubber friction behavior under different operating conditions; the inclusion of force equilibriums in determining the detailed dynamic friction states of the tread; the range of operating scenarios to which the model can be applied as well as the related accuracy.

To improve these shortcomings, we developed an analytical model to investigate tire tread friction characteristics under various load and driving speed conditions. Modified Kelvin–Voigt elements with inertia components were employed to capture the dynamic friction states of tread rubber. The elasticity of tread elements is adaptable to load. Both the effects of the load and driving speed were considered in determining the friction behavior of tread rubber. Moreover, a 2D contact patch and the associated contact pressure were utilized to reflect a more realistic contact state of the tread, especially in cornering situations. The reliability of the proposed method under different operating conditions was experimentally validated on an indoor test rig using the Grosch wheel (a miniaturized solid rubber wheel). This paper is structured as follows, the detailed modeling methodology is illustrated in Section 2. Section 3 outlines the method for identifying the model parameters. In Section 4, we validate the proposed model with experimental data for various loads and driving speeds. In addition, comparative studies with reference models are explored. Finally, the insights gained from our research are summarized in Section 5.

## 2. Modeling concept

### 2.1. Physical analysis

The brush theory is commonly used in developing analytical tire tread friction models. A typical brush-type model assumes that a tire tread is composed of numerous massless elastic bristles, with their base points connected to the tire tread base and tip points touching the road surface. These bristles do not interfere with each other and follow the relative movement between the tire tread base and the road surface. The brush theory provides a simple approach to tire tread friction modeling, but conventional brush-type models cannot capture rubber dynamic friction behavior observed in experiments, such as the transition progress between the sticking and sliding states in rubber friction [31].

In this paper, a modified Kelvin–Voigt element with an inertial component is used as a viscoelastic bristle to capture the dynamic friction response of the tread element, as schematically depicted in Fig. 1. The frictional shear stress  $\tau$  between the bristle and the road surface is in a balance with the dynamic force response of the bristle, which consists of three components, elastic part  $\tau_k$ , damping part  $\tau_c$ , and inertia part  $\tau_m$ , as demonstrated in Eq. (1).

$$\tau = \underbrace{k \delta}_{\tau_k} + \underbrace{c \frac{d\delta}{dt}}_{\tau_c} + \underbrace{m \frac{d^2\delta}{dt^2}}_{\tau_m} \quad (1)$$

Where  $\delta$  represents the horizontal deformation of the bristle.  $k$ ,  $c$  and  $m$  refer to the elasticity, damping coefficient, and inertia of the tread rubber per unit contact area, respectively.

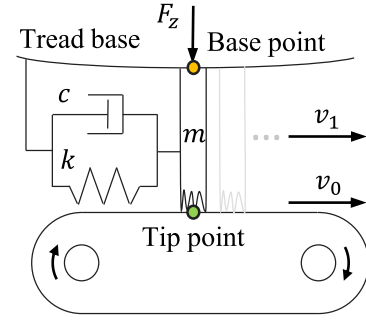


Fig. 1. Viscoelastic element in the modeling. Tip point: in green. Base point: in orange.  $v_0$  is the velocity of the road surface and  $v_1$  is the driving velocity of the tread base. The element is deflected as a result of the velocity difference between  $v_0$  and  $v_1$ .

The anisotropy of tire tread rubber is introduced by incorporating the modified Kelvin–Voigt element in the longitudinal and lateral directions of the tire, respectively, whose elasticities are related to each other as expressed in Eq. (2). Since these two Kelvin–Voigt elements represent the same tread element, they share the same inertia and friction law to maintain a concise physical interpretation.

$$k_x = \varphi k_y \quad (2)$$

Where  $k_x$  and  $k_y$  represent the value of  $k$  in tire longitudinal and lateral directions, respectively.  $\varphi$  serves as an anisotropy-related factor between  $k_x$  and  $k_y$ .

To consider the variation of tire cornering stiffness<sup>1</sup> per unit load against the applied load [32], which may arise from the changes in the internal friction within rubber compounds as well as the contact status between the tire and the road surface, the elasticity of the Kelvin–Voigt element is linearly adjusted according to tire vertical loads, see Eq. (3).

$$k_y = k_{y0} + k_{y1} F_z \quad (3)$$

Where  $F_z$  is the tire load.  $k_{y0}$  represents the default lateral elasticity of tread elements per unit contact area and  $k_{y1}$  is a load-related factor. Both  $k_{y0}$  and  $k_{y1}$  need to be determined based on experiments.

### 2.2. Force equilibrium of viscoelastic bristles

To characterize the contact status of the viscoelastic bristles in the grounding area, a 2D rectangle contact patch with a length of  $2a$  and a width of  $2b$  is incorporated, and the coordinate system is depicted in Fig. 2. At the leading edge of the tire contact patch, the bristles are in contact with the road surface. Then, the tip of the bristles follows the motion of the road surface until sliding occurs, while the base of the bristles tracks the motion of the tire tread base, and this speed difference leads to the tread deformation.

In cornering scenarios of a vehicle, as shown in Fig. 3, tires undergo a yaw motion apart from a nonzero sideslip angle, leading to additional speed differences between tire tread elements and the road surface. For a bristle at position  $(x, y)$  within the tire imprint, the resulting relative velocities between its tip point and base point in the longitudinal and lateral directions are given by Eqs. (4). The relative velocity that produces a positive deflection is defined as positive.

$$\begin{cases} v_{rx} = \omega r_e + \omega_z(y + \delta_y) - v_0 \cos \alpha \\ v_{ry} = -\omega_z(x + \delta_x) - v_0 \sin \alpha \end{cases} \quad (4)$$

Where  $\alpha$  denotes the sideslip angle.  $\omega$  refers to angular velocity of the tire.  $r_e$  represents the tire's dynamic radius.

<sup>1</sup> the gradient of the tire side force to sideslip angle at zero degrees.

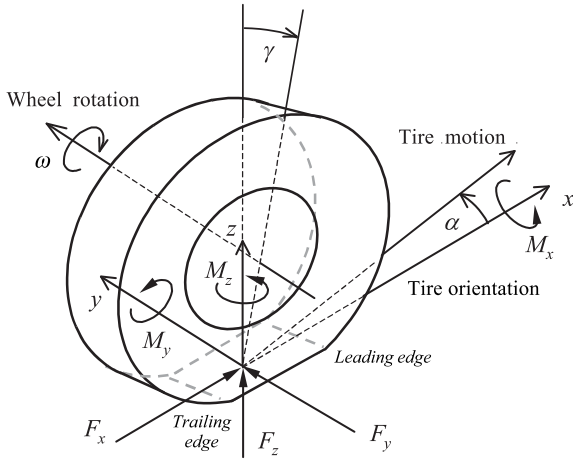


Fig. 2. Tire coordinate system.

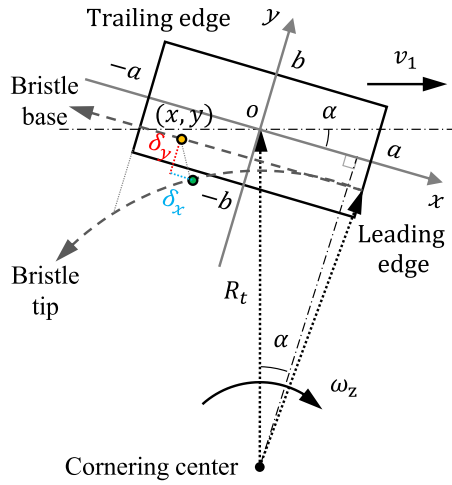


Fig. 3. The deformation of tire tread elements in the cornering motion (top view on the contact patch).  $\omega_z$  denotes the yaw velocity of the tire.  $\delta_x$  and  $\delta_y$  correspond to the longitudinal and lateral deflections of the element at position  $(x, y)$ , respectively.

As long as the friction force remains within the limits of achievable friction, the bristle adheres to the road surface. The values of  $\delta_x$  and  $\delta_y$  arise from the integration of  $v_{rx}$  and  $v_{ry}$  over traveling distance, respectively, as shown in Eqs. (5).

$$\begin{cases} \delta_x = - \int_{x_0}^x \frac{v_{rx}}{\omega r_e} dx \\ \delta_y = - \int_{x_0}^x \frac{v_{ry}}{\omega r_e} dx \end{cases} \quad (5)$$

Where  $x_0$  denotes the longitudinal position of entering the adhesion zone. The negative sign represents the direction of the deformation.

In accordance with Eq. (1), the bristle's ability to maintain its motion relies on the equilibrium between the frictional shear stress and the dynamic force response driven by its elasticity, damping, and inertia properties. In the sticking situation, this force balance is given by Eqs. (6).

$$\begin{cases} \tau_x = k_x \delta_x + c_x v_{rx} + m \frac{d v_{rx}}{dt} \\ \tau_y = k_y \delta_y + c_y v_{ry} + m \frac{d v_{ry}}{dt} \end{cases} \quad (6)$$

Once the total tangential shear stress,  $\sqrt{\tau_x^2 + \tau_y^2}$ , exceeds the available friction, the bristle detaches from the road surface and starts to

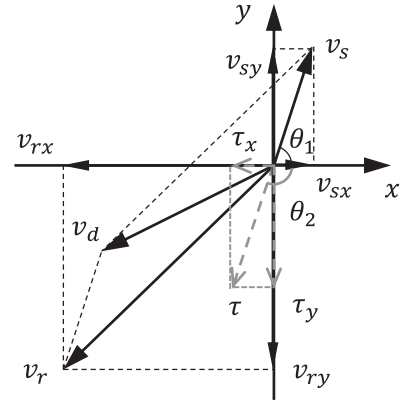


Fig. 4. Bristle kinematics with respect to the road surface in the sliding situation.  $v_d$  and  $v_s$  denote the deformation velocity and the sliding velocity of the bristle, respectively.  $\theta_1$  and  $\theta_2$  represent the orientation of the sliding velocity and the total shear stress, respectively.

slide, leading to a sliding velocity. This situation is schematically shown in Fig. 4, and the longitudinal and lateral deforming velocities of the bristle are obtained with Eqs. (7).

$$\begin{cases} \frac{d \delta_x}{dt} = v_{rx} + v_s \cos \theta_1 \\ \frac{d \delta_y}{dt} = v_{ry} + v_s \sin \theta_1 \end{cases} \quad (7)$$

In this scenario, the frictional shear stress is regulated by the kinetic CoF between the bristle and the road surface as well as the associated contact pressure, as depicted in Eqs. (8).

$$\begin{cases} \tau_x = \mu p \cos \theta_2 \\ \tau_y = \mu p \sin \theta_2 \end{cases} \quad (8)$$

Where  $\mu$  represents the kinetic CoF, which is a function of the sliding velocity and contact pressure. This will be clarified in Section 2.3.  $p$  denotes the contact pressure between the bristle and the road surface.

The sliding alters the deformation velocity of the bristle  $v_d$  and the associated friction force. As the bristle starts to slide, the force balance previously present in the sticking zone (Eqs. (6)) breaks down. This breakdown is replaced by a new force equilibrium governed by the kinetic friction, in which  $v_s$  converges to a value where the corresponding friction can sustain the ongoing motion of the bristle. As shown in Eqs. (9), the longitudinal and lateral force equilibrium of the bristle is governed by a pair of second-order ordinary differential equations (ODEs), whose initial conditions are inherited from the final state of the bristle in the preceding adhesion zone.

$$\begin{cases} \frac{d^2 \delta_x}{dt^2} = \frac{1}{m} \left( \tau_x - k_x \delta_x - c_x \frac{d \delta_x}{dt} \right) \\ \frac{d^2 \delta_y}{dt^2} = \frac{1}{m} \left( \tau_y - k_y \delta_y - c_y \frac{d \delta_y}{dt} \right) \end{cases} \quad (9)$$

The dynamic system described by Eqs. (9) contains two equations but three unknown variables,  $v_s$ ,  $\theta_1$  and  $\theta_2$ , making it unsolvable. This challenge is frequently encountered in tire models that incorporate velocity-dependent friction laws [11,14,16,24,33]. One typical solution is to employ a separate friction law in the longitudinal and lateral directions, respectively. However, this would imply that a bristle could be further divided into two distinct sub-bristles, each with different friction properties. This subdivision deviates from the physical interpretation of bristles and compromises the basic physical meaning of the bristle as representing the tread rubber. To form physically well-defined tire tread elements, this paper employs a single, uniform friction law. In this case, the maximum dissipation rate principle [34] is introduced to

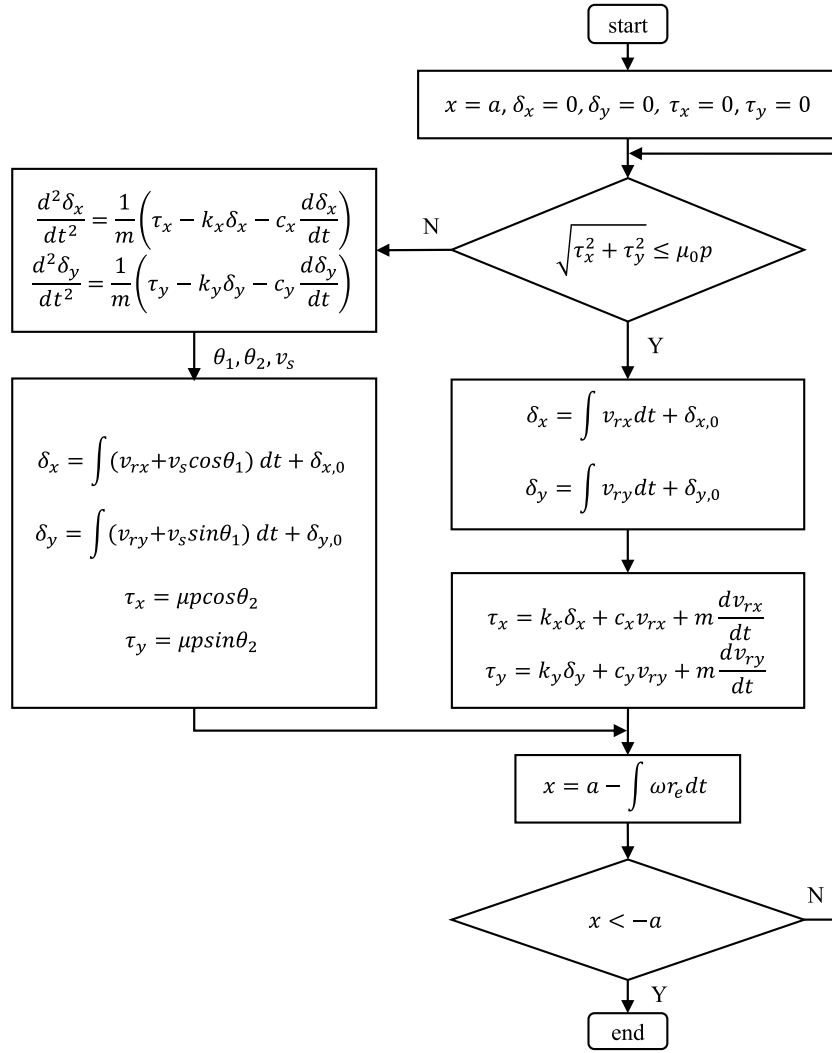


Fig. 5. Flow chart showing the process of identifying bristle's dynamic status.  $\delta_{x,0}$  and  $\delta_{y,0}$  represent the longitudinal and lateral deformation of the bristle inherited from the last iteration, respectively.

regulate  $\theta_1$  and  $\theta_2$  to maximize the dissipated frictional power density  $P_f$ , as described in Eq. (10).

$$P_f = \tau_x v_{sx} + \tau_y v_{sy} \quad (10)$$

By combining Eqs. (8) and Eq. (10), we obtain

$$P_f = \mu p v_s \cos(\theta_1 - \theta_2). \quad (11)$$

It can be seen that the frictional shear stress is collinear with the sliding velocity when utilizing a single, uniform friction law, as indicated by Eq. (12).

$$\theta_1 - \theta_2 = \pi \quad (12)$$

The processing procedure for identifying the dynamic status of bristles across the contact patch is summarized in Fig. 5. Following this identification, the dynamic states of bristles are determined for both the adhesion and sliding zones. By integrating shear stresses throughout the contact area, the global tire tread friction forces can be obtained.

### 2.3. Friction law

In the present study, the Savkoor friction law is utilized to describe rubber kinetic friction against the sliding velocity, as shown in Eq. (13). This choice is advantageous as the Savkoor law fits well with the rubber friction master curve [35–37], which illustrates the rubber friction

characteristics over a wide range of sliding velocities and temperatures. In accordance with the Savkoor friction law, as schematically shown in Fig. 6, the maximum attainable CoF is  $\mu_0$  when no sliding occurs. Otherwise, when sliding emerges, the CoF increases with sliding velocity until it reaches the maximum CoF,  $\mu_m$ , at a characteristic sliding velocity  $v_m$ . Thereafter, the CoF asymptotically decreases to  $\mu_0$ , as the sliding velocity continues to increase. Since  $v_m$  is typically small and the propagation of sliding is hindered by the resultant CoF when the sliding velocity falls below  $v_m$ , a rubber element is only characterized as sliding when its sliding velocity exceeds  $v_m$  in the subsequent discussions.

$$\mu_s = \mu_0 + (\mu_m - \mu_0) \cdot \exp\left(-h^2 \log_{10}^2\left(\frac{v_s}{v_m}\right)\right) \quad (13)$$

On the other hand, the measured CoF of rubber compounds decrease with the applied load, forming a load dependency effect [35,38,39]. Given that the original Savkoor friction law does not account for this load dependency, an adjusting factor related to the contact pressure is introduced to improve the friction law, as depicted in Eq. (14). To prevent an excessively large CoF value at very low contact pressure, a cut-off is implemented for the adjusting factor. Specifically, the contact pressure is set to  $p_0$  when it is smaller than this value. The eventual friction law is the product of  $\mu_s$  and  $sat(p)$ .

$$sat(p) = \left(\frac{p}{p_{ref}}\right)^{-q} \quad (14)$$

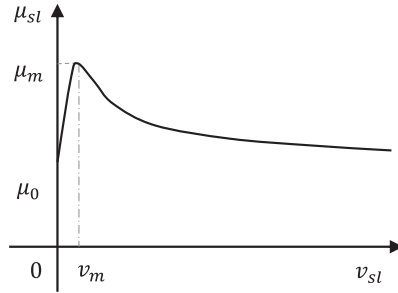


Fig. 6. Schematics of the Savkoor friction law.

Where  $p_{ref}$  is a reference pressure,  $q$  denotes the declining rate of  $sat(p)$ .

### 2.4. Contact pressure distribution

Tire-road contact pressure is important to identify the dynamic states of the bristles, e.g., the position where the bristles start to slide. In this study, we utilize a parabolic-derived pressure model from literature [40], originally developed for 1D contact patch analysis, and extend it to the lateral direction to build up a 2D contact pressure.

The modeling process consists of two steps. First, a tire's normal load is distributed along the longitudinal direction, as illustrated in Eq. (15) to (18). In this way, we obtain a line load density distributed along the longitudinal position  $x$  of the imprint,  $f_z(x)$ . Second, at each longitudinal position,  $f_z(x)$  is further distributed laterally, as shown in Eq. (19), yielding a 2D contact pressure distribution over the entire contact patch.

$$f_z(x) = \frac{F_z}{2a} \cdot g_x\left(\frac{x}{a}\right) \quad (15)$$

$$g_x(\xi_x) = A_x(1 - \xi_x^{2n_x})(1 + \lambda_x \xi_x^{2n_x})(1 - B_x \xi_x) \quad (16)$$

$$A_x = \frac{(2n_x + 1)(4n_x + 1)}{2n_x(4n_x + 1 + \lambda_x)} \quad (17)$$

$$B_x = \frac{3(2n_x + 3)(4n_x + 3)(4n_x + 1 + \lambda_x)}{(2n_x + 1)(4n_x + 1)(4n_x + 3 + 3\lambda_x)} \cdot \frac{x_e}{a} \quad (18)$$

Where  $\xi_x = x/a$  with  $\xi_x \in [-1, 1]$  denotes the relative longitudinal coordinate in the imprint. The function  $g_x(\xi_x)$  manages the shape of the pressure distribution. Thereof, the parameters  $n_x$  and  $\lambda_x$  are two shape-adjusting factors to be adapted based on measurements.  $A_x$  and  $B_x$  are two regulation parameters that guarantee the satisfaction of the boundary conditions described in Eqs. (20).  $x_e$  refers to the longitudinal distance between the center of pressure<sup>2</sup> (CoP) and the geometric center of the imprint.

$$p(x, y) = \frac{f_z(x)}{2w(x)} \cdot g_y\left(\frac{y}{w(x)}\right) \quad (19)$$

Where  $w(x)$  represents half of the imprint width at the longitudinal position  $x$ . The function  $g_y(y/w(x))$  has the same expression as  $g_x(x/a)$ , but employs a separate set of parameters, namely  $n_y$ ,  $\lambda_y$ ,  $y_e(x)$ ,  $A_y$ , and  $B_y$ . In particular, for a contact strip laterally sliced at longitudinal position  $x$ ,  $y_e(x)$  represents the lateral distance between the CoP of this strip and the geometric center of the complete imprint. For the rectangular imprint utilized in the proposed model,  $y_e(x)$  is simplified as a constant.<sup>3</sup> Then the constraint depicted in Eq. (21) is fulfilled. An

<sup>2</sup> the point where the sum of the road supporting force is concentrated.

<sup>3</sup> if the imprint is non-rectangular, this simplification may cause an error: for those strips around the leading and trailing edges,  $y_e(x)$  is larger than half of their width.

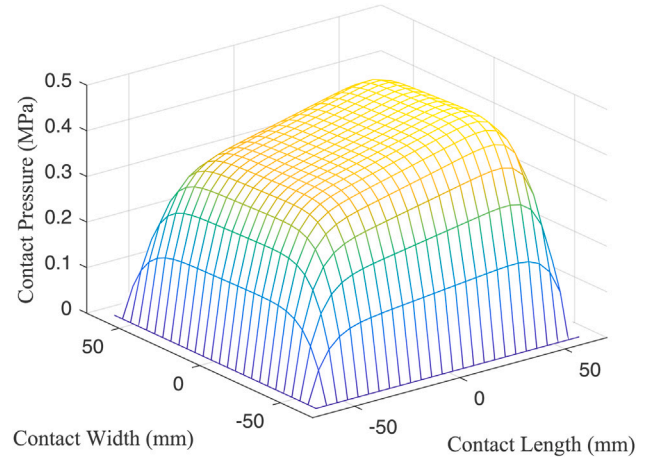


Fig. 7. Contact pressure distribution with parameters:  $n_x = 2$ ,  $\lambda_x = 1$ ,  $x_e = 3.5$  mm,  $n_y = 1.5$ ,  $\lambda_y = 1$ ,  $y_e = 0$  mm (Example in a load of 5000 N, and imprint size of 126 mm × 126 mm).

example of the resulting contact pressure distribution is given in Fig. 7.

$$\begin{cases} \int_{-a}^a f_z(x) dx = F_z \\ \int_{-a}^a f_z(x)x dx = F_z x_e \end{cases} \quad (20)$$

$$\int_{-a}^a \int_{-b}^b p(x, y) dy dx = F_z y_e \quad (21)$$

## 3. Parameter identification

### 3.1. Test rig setup

The tests and following experimental validation were conducted on the Grip and Abrasion Test Stand (GAT), which was developed by the Institute of Vehicle System Technology, Karlsruhe Institute of Technology (KIT). Similar to the well-known Laboratory Abrasion & Skid Tester (LAT 100), GAT is a compact indoor test bench designed to investigate the friction characteristics and abrasability performance of rubber specimens, as shown in Fig. 8. Both artificial surfaces such as sandpaper and safety walk,<sup>4</sup> and drilled road samples of real road surfaces can be employed. On the other hand, GAT offers the flexibility to use rubber blocks and Grosch wheels for testing. With a solid rubber wheel, the wheel is in free rolling<sup>5</sup> and its sideslip angle is adjustable. The main technical specifications of GAT are listed in Table 1.

To better approximate the operating conditions of full-size tires and reduce shocks from oversized asperities of road surfaces, the Grosch wheel and safety walk surface are utilized in the following measurements.

### 3.2. Parameters calibration

The parameters involved in the proposed model were grouped into two categories based on their functions: imprint-related and friction-related. Certain parameters, like the imprint length and width, were calibrated through measurements. However, some parameters, such as those related to contact pressure distribution and friction, are challenging to measure directly. For these cases, the values were fine-tuned using the least-squares method to minimize the difference between

<sup>4</sup> similar to sandpaper but generally with larger grains on the surface.

<sup>5</sup> no braking or driving torque acts on the wheel.

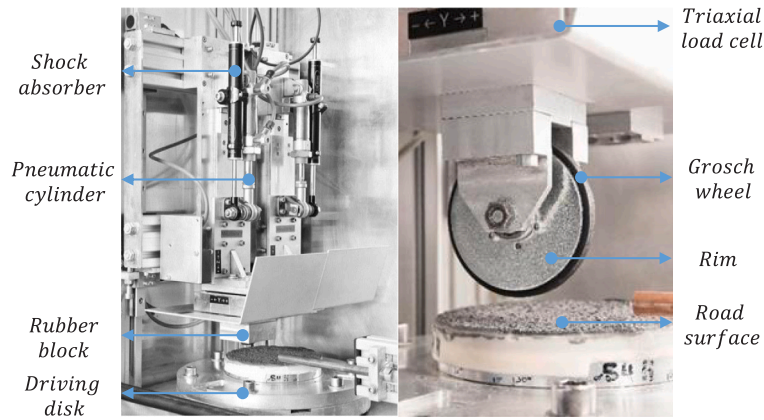


Fig. 8. Setup of the Grip and Abrasion Test Stand.

Table 1  
Structural parameters of the Grip and Abrasion Test Stand.

Items	Value	Unit
Road disk radius	75	mm
Track radius $R_t$	60	mm
Wheel radius $r_e$	36	mm
Wheel width $2b$	18	mm
Rim radius	30	mm
Driving speed	$[0 \pm 1000]$	r/min
Sideslip angle	$[0 \pm 37.5]$	°
Force $F_x, F_y, F_z$	$[0 \pm 200]$	N

experimental observations and the associated model results. The root mean squared error (RMSE), as described in Eq. (22), between the model and the observations is utilized to evaluate the model accuracy.

$$RMSE = \sqrt{\frac{\sum_{i=1}^n (\hat{y} - y)^2}{n}} \quad (22)$$

Where  $\hat{y}$  and  $y$  correspond to estimated and experimental values, respectively.  $n$  is the number of data samples.

Due to the flat cross-section of the Grosch wheel, the imprint width remained almost constant at 18 mm under different vertical loads, as shown in Table 2. The dependency of the contact length on vertical loads was described using a regression model as depicted in Eq. (23).

$$a = a_1 F_z^{a_2} + a_3 \quad (23)$$

The contact pressure in the imprint was measured using pressure-sensitive membranes, and the result is shown in Fig. 9. This experimental result was used to determine the parameters of the contact pressure model.

The friction-related parameters were characterized by allowing the model to better align with the measured lateral force of the Grosch wheel under load- and speed-varying conditions, as listed in Table 3. For both conditions, the sideslip angle of the Grosch wheel linearly swept from  $0^\circ$  to  $37.5^\circ$ , and then back to  $0^\circ$ . The identified parameters are listed in Table 4.

## 4. Results and discussion

This section explores the tread rubber friction characteristics under varying loads and speeds using the proposed model. Model results are validated against experiments with the Grosch wheel, and the dynamic friction behavior of the tread elements revealed by the model is used to interpret tread friction performance. Finally, the pivotal considerations necessary for the tire tread friction model to capture tread friction behaviors are examined through comparisons with reference models.

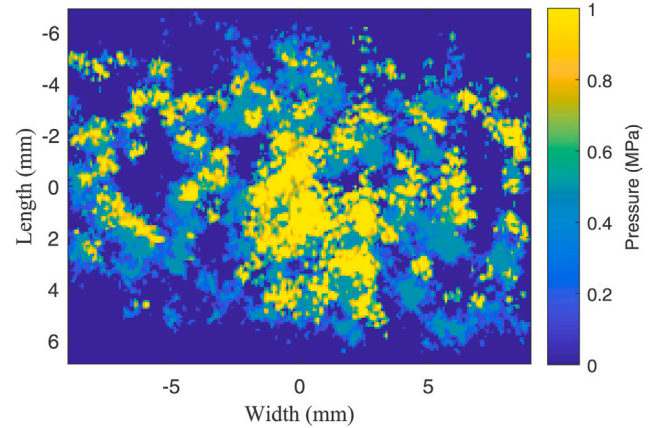


Fig. 9. Contact pressure distribution between the Grosch wheel and the road surface at a load of 75 N.

### 4.1. Load varying conditions

In load-varying conditions, the driving speed remained consistent at 1 m/s, which corresponds to a velocity of 35 km/h for a full-size passenger car tire (255/40 R20) regarding the excitation frequency emanating from the road surface [26,41]. Concerning the local movement of tread rubber, the inner and outer edges of the wheel move at different speeds due to the curved track on GAT. The bristles at the inner edge are under traction while those at the outer edge are in braking. As a result, this cornering effect makes bristles located in the edge region experience additional longitudinal forces and fall into sliding earlier than those at the centerline, as graphically depicted by the model outcomes in Fig. 10.

Due to the cornering effect, the Grosch wheel yields a nonzero side force when the sideslip angle is zero. Additionally, the sideslip angle at which the Grosch wheel exerts zero side force, denoted by  $\alpha|_{F_y=0}$ , is also not zero. Specifically, the side force of the Grosch wheel  $F_y$  reaches zero when the sum of lateral shear stresses generated from the front of the contact patch balances with the sum of lateral stresses generated from the rear zone, as demonstrated in Fig. 11.

To evaluate the influence of vertical loads and cornering radius on  $\alpha|_{F_y=0}$ , the deflection state of the bristles situated at the imprint centerline are assessed. Since the value of  $\alpha|_{F_y=0}$  is relatively small, the sliding of the bristles is disregarded for the sake of simplification. Then, the lateral deflection of the bristles at longitudinal position  $x$  can be determined according to Eqs. (5), see Eq. (24).

$$\delta_y = \frac{a^2 - x^2}{2R_t \cos \alpha} - (a - x) \tan \alpha \quad (24)$$

**Table 2**  
Ink measurements of the Grosch wheel under various vertical loads.

Load (N)	30	64	86	118	147	184
Imprint						

**Table 3**  
Friction measurements with the Grosch wheel on GAT.

Conditions	Load (N)	Speed (m/s)	Sideslip angle (°)
Load varying	40/60/100/120	1	[0 37.5]
Speed varying	60	0.25/0.5/1/2	[0 37.5]

**Table 4**  
Identified model parameters.

Friction			Imprint		
Item	Value	Unit	Item	Value	Unit
$\mu_0$	0.02	–	$a_1$	1.03	–
$\mu_m$	1.15	–	$a_2$	0.44	–
$v_m$	23.47	mm/s	$a_3$	0	–
$h$	0.23	–	$b$	9	mm
$p_0$	0.02	MPa	$n_x$	0.74	–
$p_{ref}$	0.39	MPa	$\lambda_x$	0	–
$q$	0.28	–	$x_e$	0.26	mm
$\phi$	0.32	–	$n_y$	1	–
$k_{y0}$	0.37	MPa/mm	$\lambda_y$	0.03	–
$c_x$	$1.78 \times 10^{-7}$	MPa/(mm/s)	$y_e$	0	mm
$c_y$	$1.40 \times 10^{-4}$	MPa/(mm/s)			
$m$	$7.64 \times 10^{-10}$	MPa/(mm/s <sup>2</sup> )			
$k_{y1}$	-0.001	1/mm <sup>3</sup>			

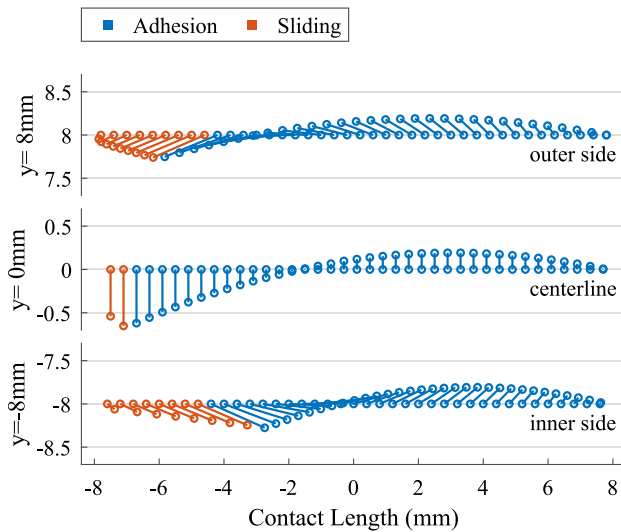


**Fig. 10.** Top view on the tangential deflection of bristles at three representative lateral positions of the imprint ( $y = 8 \text{ mm}, 0 \text{ mm}, -8 \text{ mm}$ ). Operating condition: ( $F_z = 100 \text{ N}, \alpha = 3^\circ, v_0 = 1 \text{ m/s}, R_t = 60 \text{ mm}$ ). Leading edge: right side. Trailing edge: left side.

According to the definition of  $\alpha|_{F_y=0}$ , the side force reaches zero when the sideslip angle fulfills

$$\int_{-a}^a \delta_y dx = \frac{2a^3}{3R_t \cos \alpha} - 2a^2 \tan \alpha \rightarrow 0. \quad (25)$$

Then, the value of  $\alpha|_{F_y=0}$  can be obtained, as described in Eq. (26). It is clear that the value of  $\alpha|_{F_y=0}$  reveals a positive correlation with the contact length  $2a$ , while showing a negative correlation with the

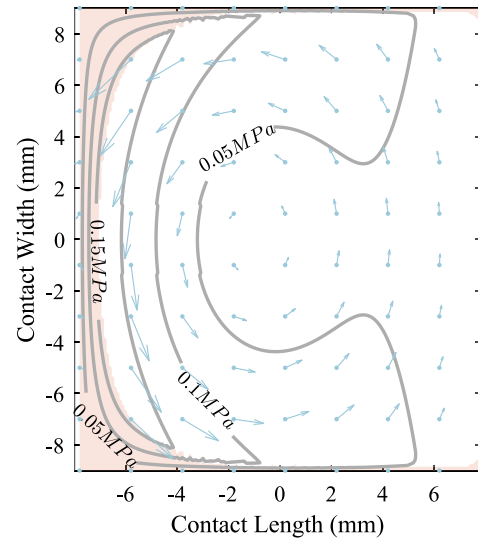


**Fig. 11.** Tangential shear stress distribution of bristles on the imprint. Operating condition: ( $F_z = 100 \text{ N}, \alpha = 3^\circ, v_0 = 1 \text{ m/s}, R_t = 60 \text{ mm}$ ). Brown area: the sliding zone. Light blue arrows: shear stress vectors. Contour line: magnitude of the total tangential shear stress. Leading edge: right side. Trailing edge: left side.

cornering radius  $R_t$ .

$$\alpha|_{F_y=0} = \arcsin\left(\frac{a}{3R_t}\right) \quad (26)$$

To validate the applicability of the proposed model in estimating tire tread friction force under various vertical loads, the comparison between experiments and the associated model results are collected and compared in Fig. 12. On the one hand, it can be seen that the model presents a favorable agreement with the experiments across

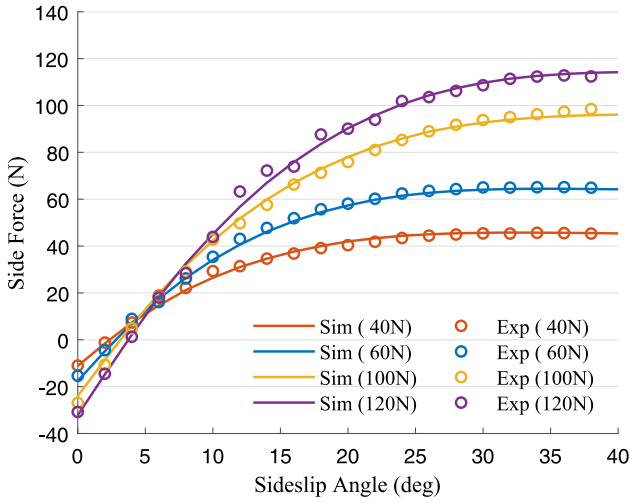


Fig. 12. Simulated and experimental side force under various vertical loads with the resulting RMSE of 1.74. Operating condition: ( $v_0 = 1$  m/s,  $R_t = 60$  mm).

both low and high load conditions, as well as for small and large sideslip angles. On the other hand, the experiments confirm that  $\alpha|_{F_y=0}$  increases with the vertical load as implied by Eq. (26). The maximum side force increases to a lesser extent in comparison to the vertical load. Therefore, it can be concluded that the maximum achievable CoF of the wheel declines with the vertical load. Both effects are precisely captured by the model.

Apart from capturing the tread friction force, further efforts are made to examine the benefits of including load-related factors into the model, and two reference models are used for comparison, denoted by  $M_k$  and  $M_{\mu_p}$ , respectively. The main differences between these two models and the proposed model are listed below.

$M_k$  : the stiffnesses of the bristles are independent of the load, namely the variable  $k_{y1}$  in Eq. (3) is set to 0.

$M_{\mu_p}$  : the load dependency of the friction law is neglected, typically the factor  $sat(p)$  is set to 1.

The parameters of  $M_k$  and  $M_{\mu_p}$  are listed in Table A.6 (Appendix A), and the associated results are enclosed in Figs. B.17(a) and B.18(a) (Appendix B). The model  $M_k$  shows a good correlation with the experiments at high sideslip angles but performs poorly at low sideslip angles. Specifically, the simulated cornering stiffness is smaller than the measurements under low load conditions, while under high load conditions, it is larger. As for the model  $M_{\mu_p}$ , its discrepancies with the measurements primarily emerge at high sideslip angles, where the simulated side forces are overestimated under high loads and underestimated under low loads. The model  $M_k$  and  $M_{\mu_p}$  underscore that, for the load-varying conditions, the consideration of the load dependency of the friction law helps to improve model performance at high sideslip angles, while the inclusion of the load dependency of the bristle's elasticity helps to enhance model at low sideslip angles.

#### 4.2. Speed varying conditions

In speed-varying conditions, the vertical load was maintained at 60 N. This wheel load corresponds to a 2.6 bar contact pressure, which is a practical approximation of the value exhibited by normal passenger car tires. Due to the viscoelastic effect, the change in driving speed influences the friction force response of tread elements, which in turn also affects their sticking and sliding status on the road surface. Taking tread elements at the centerline of the contact patch as an example,

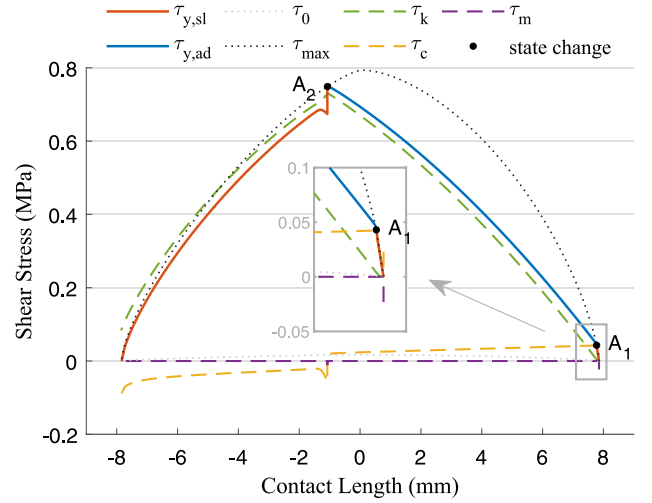


Fig. 13. Local friction states of the bristles and their force composition under operating condition ( $F_z = 100$  N,  $\alpha = 10^\circ$ ,  $v_0 = 1$  m/s,  $R_t = 60$  mm).  $\tau_{y,sl}$ : lateral shear stress in sliding zones.  $\tau_{y,ad}$ : lateral shear stress in adhesion zone.  $\tau_0$ : stiction limit.  $\tau_{max}$ : maximum attainable friction limit.  $\tau_k$ ,  $\tau_c$  and  $\tau_m$  derive from Eq. (1). Leading edge: right side. Trailing edge: left side.

their local friction states are depicted in Fig. 13, in which the contact area consists of three distinct zones: an adhesion zone (from  $A_1$  to  $A_2$ ) and two sliding zones (the first from the leading edge to  $A_1$ , and the second from  $A_2$  to the trailing edge).

Within the adhesion zone, the presence of the viscoelastic effect increases the lateral shear stress of the elements in the adhesion zone  $\tau_{y,ad}$  when the elements move away from their initial position at a larger speed, which further leads to a smaller adhesion area due to the finite friction limit. As a result, a higher driving speed produces a reduced adhesion area in the contact patch for a given sideslip angle, as demonstrated in Fig. 14. Within the sliding zones, the influence of the viscoelastic effect on the lateral shear stress of the elements in the sliding zone  $\tau_{y,sl}$  is non-monotonic. In the first sliding zone, where the bristles move away from their initial positions, the presence of the viscoelastic effect results in an augmentation of  $\tau_{y,sl}$ . Conversely, within the second sliding zone, as the bristles retreat back to their original positions, the viscoelasticity causes a reduction in  $\tau_{y,sl}$ . Notwithstanding these two opposing influences, the value of  $\tau_{y,sl}$  remains consistent with the stipulations of the friction law that governs sliding conditions.

Since a stronger viscoelastic effect contributes to an increased adhesive shear stress  $\tau_{y,ad}$  but a reduced adhesion area, the side force generated from the adhesion zone, denoted as  $F_{y,ad}$ , follows a quadratic relationship with driving speeds.  $F_{y,ad}$  increases with higher driving speeds when the viscoelastic effect's impact on  $\tau_{y,ad}$  counterbalances the decline in the adhesion area, otherwise,  $F_{y,ad}$  decreases. A similar relationship exists between the side force produced within the sliding zones, denoted as  $F_{y,sl}$ , and the driving speed. Elevated driving speeds lead to a larger sliding area but a smaller kinetic CoF. As a consequence,  $F_{y,sl}$  also presents quadratic variations linked to driving speeds. In summary, the impact of driving speeds on side forces varies depending on the sticking and sliding states of the contact patch. For large sideslip angles, the sliding zones constitute the major proportion of the contact patch, higher driving speeds result in lower side forces. Conversely, for relatively small sideslip angles, the adhesion zone dominates the contact patch, and greater driving speeds lead to larger side forces, as indicated in Fig. 15.

Fig. 16 introduces the comparison between the proposed model and experiments at different driving speeds. Despite some experimental deviation, the measured side force closely follows the trend revealed by the proposed model. As the driving speed increases, the wheel side force exhibits a steeper ascent concerning sideslip angles, ultimately

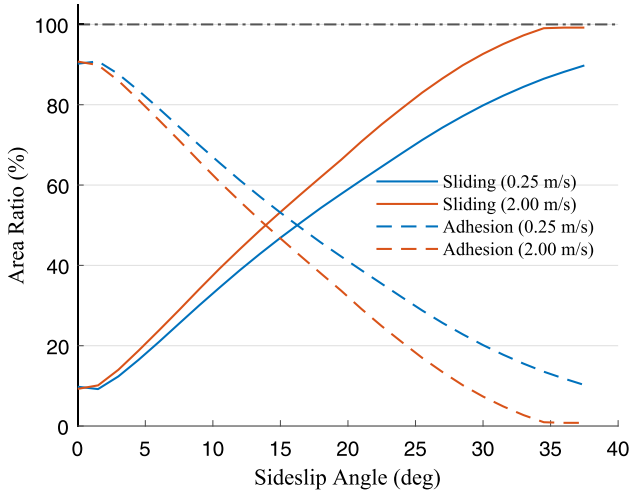


Fig. 14. The ratio of the adhesion and sliding area in the entire contact patch under different driving speeds. Operating condition: ( $F_z = 60\text{ N}$ ,  $R_t = 60\text{ mm}$ ). Since the track is in a circular shape, the adhesion zone does not fully occupy the contact patch at zero sideslip angle.

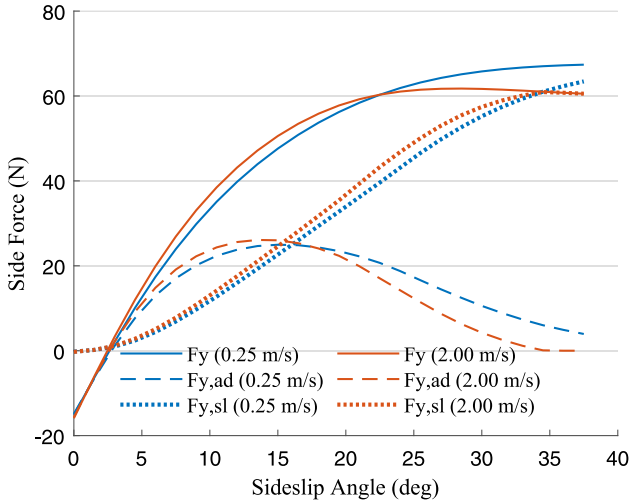


Fig. 15. The contribution of the side force generated from the adhesion zone ( $F_{y,ad}$ ) and the side force generated from the sliding zones ( $F_{y,sl}$ ) to the total side force under different driving speeds. Operating condition: ( $F_z = 60\text{ N}$ ,  $R_t = 60\text{ mm}$ ).

reaching a smaller maximum value compared to scenarios with lower driving speeds. Remarkably, the disparity in side force between conditions of 0.25 m/s and 2 m/s reaches up to approximately 8%, which occurs not only at high sideslip angles above  $35^\circ$  but also at moderate sideslip angles around  $13^\circ$ .

To clarify the necessity of incorporating speed-related rubber properties in capturing tread rubber friction performance at different driving speeds, here we employ two reference models for comparison with the proposed model:  $M_c$  and  $M_{\mu_s}$ . These two models incorporate targeted modifications, as outlined below, while the rest structure retains compared to the proposed model.

$M_c$ : the conventional spring-type bristles are applied, which means the viscoelasticity of the bristles is neglected. This is equivalent to the case that the damping  $c$  and inertia  $m$  of the proposed viscoelastic element are set to 0.

$M_{\mu_s}$ : the Coulomb friction law is utilized, as described in Eqs. (27), thereby excluding the speed dependency of the friction law.

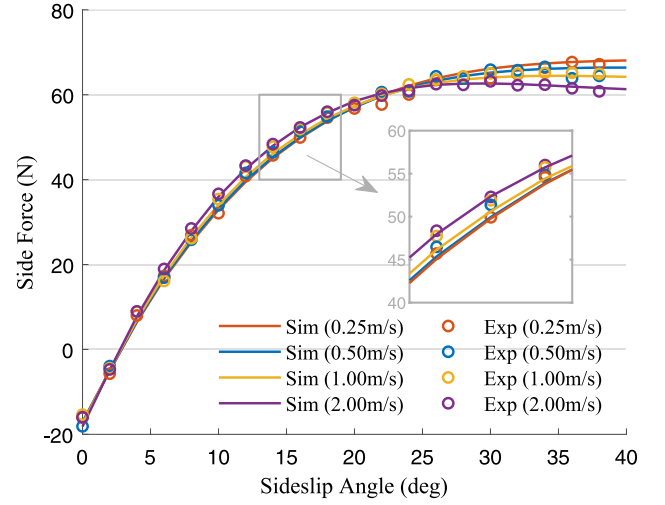


Fig. 16. Simulated and experimental side force under various driving speeds with the resulting RMSE of 1.09. Operating condition: ( $F_z = 60\text{ N}$ ,  $R_t = 60\text{ mm}$ ).

This indicates that in sliding circumstances, the friction force is constant with sliding velocities.

$$\mu_c = \begin{cases} \mu_0 & \text{if } v_s = 0 \\ \mu_m & \text{if } v_s \neq 0 \end{cases} \quad (27)$$

In the case of the model  $M_c$ , as shown in Fig. B.19(b), greater driving speeds consistently yield lower side forces, regardless of the sideslip angles. This reduction in side force becomes more pronounced as the sideslip angle increases, which is attributed to the reduced CoF under higher sliding velocities. In contrast, the model  $M_{\mu_s}$  exhibits amplified side forces at elevated driving speeds due to the viscoelastic effect, especially at low sideslip angles where the adhesion zone takes the majority of the contact patch, as depicted in Fig. B.20(b). Across all four speed scenarios, the side forces eventually converge to a constant value when sideslip angles become sufficiently large (e.g.,  $30^\circ$ ). This convergence is attributed to the limitation of the Coulomb friction law in accounting for the CoF under diverse sliding speeds.

In conclusion, the models  $M_c$  and  $M_{\mu_s}$  indicate that accounting for the viscoelastic effect is crucial for accurately reflecting the influence of driving speeds on tread friction at low sideslip angles while considering the speed-dependency of rubber friction plays a significant role in capturing this influence at relatively large sideslip angles.

#### 4.3. Comparative study

In this section, we carry out comprehensive comparative studies to explore model performance across different loads and driving speeds before and after accounting for certain influencing factors. Specifically, the speed- and load-dependency of friction law, the load dependency of bristle's elasticity, the viscoelastic effect, and the dimension of the contact patch (1D or 2D) are of interest.

In addition, the performance of another kind of viscoelastic rubber friction model, the classical LuGre model [9], is also examined with the experimental data, for additional reference. Notably, the LuGre model requires a separate set of parameters to be calibrated for each operating condition [12,42], which is not suitable to be straightly utilized in the comparison including multiple driving scenarios. Therefore, we further enhanced it by accounting for the load dependency of friction law and the load dependency of bristle's elasticity and also extended its 1D contact patch to a 2D version. Eqs. (28) demonstrate the key method for calculating the side force in the enhanced LuGre model. The global

**Table 5**  
Model performance, main considerations, and their comparable sources.

Model	Dim.	F.L.	V.E.	L.F.	L.S.	Error Index		Source
						L.V.	S.V.	
$M_0$	1D	Cou	–	–	–	2.97	3.39	[30,43]
$M_1$	1D	Sav	–	–	–	2.94	3.32	[33,44]
$M_{\mu p}$	2D	Sav	✓	–	✓	1.73	1.50	–
$M_k$	2D	Sav	✓	✓	–	1.44	1.54	[21](V.E.) <sup>a</sup>
$M_2$	1D	Sav	–	✓	✓	1.13	1.43	–
$M_c$	2D	Sav	–	✓	✓	1.04	1.39	[45](L.F.)
$M_{\mu s}$	2D	Cou	✓	✓	✓	0.97	1.21	–
$Opt$	2D	Sav	✓	✓	✓	1	1	–
$LuGre$	2D	$\mu_y$	✓	✓	✓	1.19	1.26	[46](L.F.)

Dim.: dimension of contact patch; F.L.: friction law; V.E.: viscoelastic effect; L.F.: load dependency of the friction law; L.S.: load dependency of bristle's elasticity; L.V.: load varying conditions; S.V.: speed varying conditions.

<sup>a</sup> [ref](\*): an additional consideration “\*” is added on the basis of research “ref”.

side force is calculated by integrating the lateral shear stress over the entire contact patch, as done in the proposed model.

$$\begin{cases} \frac{d\delta_y}{dt} = v_{ry} - \frac{k_y\delta_y}{\mu_y p} \cdot |v_{ry}| \\ \mu_y = sat(p) \cdot \left( \mu_0 + (\mu_m - \mu_0) \cdot \exp\left(-\left|\frac{v_{ry}}{v_{m2}}\right|^\beta\right) \right) \\ \tau_y = k_y\delta_y + c_y \frac{d\delta_y}{dt} + c_{y2}v_{ry} \end{cases} \quad (28)$$

Where  $v_{m2}$  is the Stribeck speed,  $\beta$  denotes the Stribeck exponent managing the decay rate of friction force over sliding speed,<sup>6</sup>  $c_{y2}$  is a factor representing the viscous friction.

To individually highlight the effects of the influencing factors mentioned above, apart from the four reference models introduced in Sections 4.1 and 4.2, three other typical tire models using a 1D contact patch are established, denoted by  $M_0$ ,  $M_1$ , and  $M_2$ , respectively. Compared to the proposed model, these three models do not consider the viscoelastic effect. Additionally,  $M_0$  applies the Coulomb friction law, while the other two models adopt the Savkoor friction law. Furthermore,  $M_2$  incorporates the load dependency of friction law and the load dependency of bristle's elasticity, which are not considered in the other two models. The core considerations of these reference models and their performance are summarized in Table 5, in which the proposed model is referred to as  $Opt$ .

The imprint parameters of these models remain consistent with the proposed model as listed in Table 4. Particularly, for these models using a 1D contact patch, only the parameters related to the longitudinal direction are valid. The identified friction parameters are included in Table A.6 and the associated simulation results are enclosed in Appendix B (see Figs. B.17–B.24). The accuracy of reference models is assessed using an *Error Index*, defined as the ratio of the RMSE values between these models and the proposed model  $Opt$ . A model with a lower *Error Index* means better performance. In addition, some of the utilized reference models were adapted from other studies and modified to suit our experimental conditions. Both the related comparable research and the modifications made to the reference models in relation to the original studies are listed in Table 5.

It is reasonable that the most common and traditional model  $M_0$  exhibits the lowest accuracy as it has the least considerations. Simply substituting the Coulomb friction law by a velocity-dependent friction law in  $M_0$  is not sufficient to effectively improve model performance, as indicated by  $M_1$ . However, after incorporating the load dependency of

<sup>6</sup>  $\beta$  is 0.5 in some studies [14,15] while 2 in others [9], here we determine  $\beta$  by optimization for the best performance.

the friction law and the load dependency of the bristle's elasticity, the deviation in the results of  $M_1$  can be reduced over 50%, as shown by  $M_2$ . Despite the improvements made to the LuGre model, the proposed model  $Opt$  still performs better than the enhanced LuGre model under the load- and speed-varying conditions. Other findings involving the effect of the influencing factors are listed below through comparing different models:

- (1) Speed dependency of the friction law ( $M_0 \sim M_1$ ,  $M_{\mu s} \sim Opt$ ):<sup>7</sup> This factor has a negligible effect on the model using a 1D contact patch. However, for models using a 2D contact patch, neglecting this factor leads to a 21% greater deviation in speed-varying conditions. The slight degradation in  $Opt$  relative to  $M_{\mu s}$  under load-varying conditions is due to the trade-off for better overall performance.
- (2) Load dependency of the friction law ( $M_{\mu p} \sim Opt$ ): This factor exhibits prominent influences on the accuracy of the models, neglecting it causes a 73% greater deviation in load-varying conditions and a 50% greater deviation in speed varying conditions.
- (3) Load dependency of bristle's elasticity ( $M_k \sim Opt$ ): Considering this factor prevents the deviation of the model results from increasing by 44% in load-varying conditions and 54% in speed-varying conditions.
- (4) Viscoelastic effect ( $M_c \sim Opt$ ): Accounting for this factor significantly improves model performance in speed varying conditions, avoiding a 39% increase in the deviation of the model results. Nevertheless, its impacts in the context of load-varying conditions are limited.
- (5) Dimension of the imprint ( $M_2 \sim M_c$ ): Changing the contact patch from 1D to 2D improves model performance, while this enhancement is relatively limited compared to other factors listed above. However, upon analyzing the difference in the enhancements from  $M_0$  to  $M_1$ , and from  $M_{\mu s}$  to  $Opt$ , it is evident that a 2D contact patch helps to amplify the advantages gained from considering the speed dependency of the friction law.

## 5. Conclusion

This research presents an analytical model for characterizing tire tread friction across various driving scenarios while considering its dynamic friction states. The analysis is based on Grosch wheels, but the model is also applicable to complete tires. The concept of modeling originates from the brush theory. However, instead of conventional

<sup>7</sup>  $A \sim B$ : by comparing A with B.

**Table A.6**  
Friction parameters of reference models.

Item	$M_0$	$M_1$	$M_{\mu_p}$	$M_k$	$M_2$	$M_c$	$M_{\mu_s}$	$LuGre$	Unit
$\mu_0$	1	1	0.02	0.02	0.07	0.01	0.94	0.06	–
$\mu_m$	1.01	1.01	1.18	1.16	1.08	1.12	1.01	1.18	–
$v_m$	–	306.27	21.32	23.42	23.98	24.07	–	–	mm/s
$h$	–	0.11	0.25	0.25	0.22	0.16	–	–	–
$p_0$	–	–	–	0.02	0.02	0.01	0.05	0.15	MPa
$p_{ref}$	–	–	–	0.40	0.42	0.40	0.59	0.59	MPa
$q$	–	–	–	0.30	0.26	0.31	0.32	0.19	–
$\varphi$	0.35	0.35	0.27	0.38	0.33	0.31	0.32	–	–
$k_{y0}$	0.32	0.31	0.48	0.28	0.36	0.39	0.40	0.49	MPa/mm
$c_x$	–	–	1.57	1.61	–	–	0.1	–	$10^{-6}$ MPa/(mm/s)
$c_y$	–	–	1.21	1.41	–	–	0.31	0.001	$10^{-4}$ MPa/(mm/s)
$m$	–	–	0.0009	0.0009	–	–	91	–	$10^{-10}$ MPa/(mm/s <sup>2</sup> )
$k_{y1}$	–	–	–5.59	–	–2.93	–2.93	–3.50	–4.82	$10^{-4}$ 1/mm <sup>3</sup>
$v_{m2}$	–	–	–	–	–	–	–	1630	mm/s
$c_{y2}$	–	–	–	–	–	–	–	8.56	$10^{-5}$ MPa/(mm/s)
$\beta$	–	–	–	–	–	–	–	1.21	–

spring elements, novel viscoelastic elements are incorporated. This innovative update allows us to precisely track the force equilibrium of tread elements, especially during sliding on the road surface. The elements are physically well-defined using a uniform friction law on a realistic 2D contact patch. Rubber properties such as the viscoelastic effect, anisotropy, adaptable elasticity, and load/speed dependency of the coefficient of friction are comprehensively incorporated. Experiments conducted with Grosch wheels on the Grip and Abrasion Test Stand have validated the model's reliability across a wide range of load and speed scenarios. Comparative studies indicate that the proposed model has superior accuracy than previous models under both load-varying and speed-varying conditions. Moreover, the efficacy of various decisive factors in the model's performance is assessed, as demonstrated below:

- (1) Vertical load related: Larger vertical loads lead to a decline in the maximum attainable coefficient of friction and the cornering stiffness of the rubber wheel, which necessitates the consideration of the load dependency of the bristle's elasticity and the load dependency of the friction law in modeling. The former mainly affects model performance at low sideslip angles, while the latter dominates model accuracy at high sideslip angles.
- (2) Driving speed related: Higher speeds result in larger side forces at low sideslip angles, and smaller side forces at relatively high sideslip angles. This contrasting phenomenon is attributed to the intertwined effects from the velocity dependency of the friction law and the viscoelastic effect. To accurately reflect tire friction characteristics across different speeds, it is necessary to consider both of these factors in the modeling.
- (3) Other modeling related: For both load-varying and speed-varying conditions, the deviation in the model results can be reduced by over 50% by taking into account the influence of the load on the friction law and the tread elasticity. The inclusion of the viscoelastic effect helps the proposed model avoid a 39% degradation in the speed-varying conditions. The dimension of the contact patch (1D or 2D) itself shows a limited influence on the model accuracy. However, in addition to providing an authentic depiction of the interactions between the tire tread and road surface, a 2D contact patch shows the ability to help the model reach a better level of accuracy when incorporating more refined considerations.

This research offers valuable insights into tire friction, and lays the foundation for more sophisticated tire tread friction models suitable for a variety of driving conditions. Based on the dynamic friction states derived from the actual force balance of the tread elements, further exploration of tire tread friction-related phenomena, such as tire abrasion and the emission of particulate matter from tire–road interactions, becomes possible.

### CRediT authorship contribution statement

**Meng Zhang:** Writing – original draft, Visualization, Validation, Software, Methodology, Investigation, Formal analysis, Data curation, Conceptualization. **Hans-Joachim Unrau:** Writing – review & editing, Supervision, Conceptualization. **Martin Gießler:** Writing – review & editing, Supervision. **Frank Gauterin:** Writing – review & editing, Supervision, Resources.

### Declaration of competing interest

The authors declare the following financial interests/personal relationships which may be considered as potential competing interests: Meng Zhang reports financial support was provided by China Scholarship Council. If there are other authors, they declare that they have no known competing financial interests or personal relationships that could have appeared to influence the work reported in this paper.

### Data availability

Data will be made available on request.

### Acknowledgments

The first author acknowledges support from the China Scholarship Council (CSC). We acknowledge support by the KIT-Publication Fund of the Karlsruhe Institute of Technology.

### Appendix A. Friction parameters of reference models

The friction-related parameters of the reference models are determined according to the approach described in Section 3.2.

### Appendix B. Results of reference models

The results of the reference models are numerically derived using the semi-implicit Euler method. The simulation configurations are kept identical to the proposed model, such as step length (in the space domain, 1 mm), root-finding algorithm (the Secant method), and converging tolerance ( $x : 1 \times 10^{-6}$  mm/s and  $y : 1 \times 10^{-4}$ ).

The operating condition of the wheel utilized in the following simulation are the same as the proposed model, i.e., in load varying condition: ( $v_0 = 1$  m/s,  $R_t = 60$  mm); in speed varying condition: ( $F_z = 60$  N,  $R_t = 60$  mm)

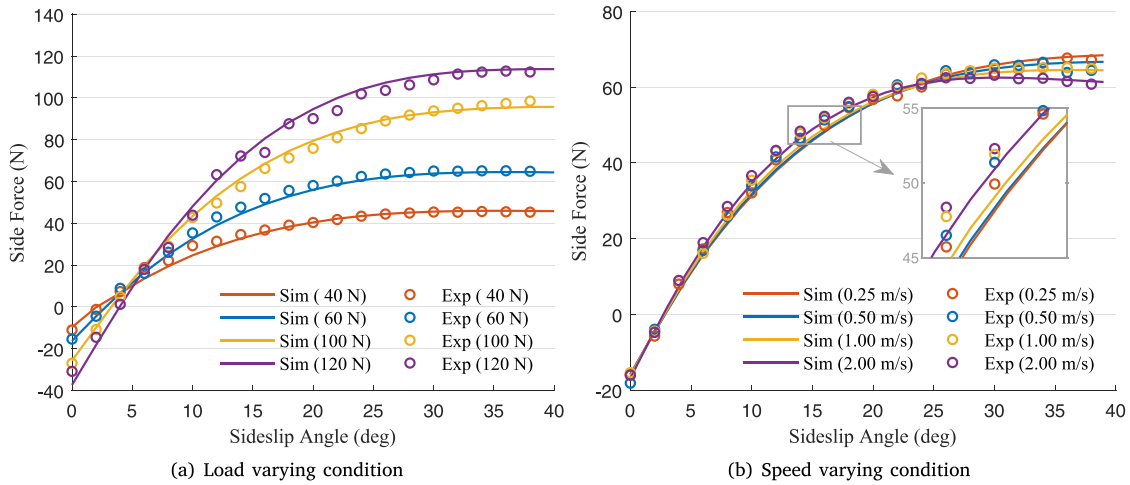


Fig. B.17. Results from model  $M_k$ .

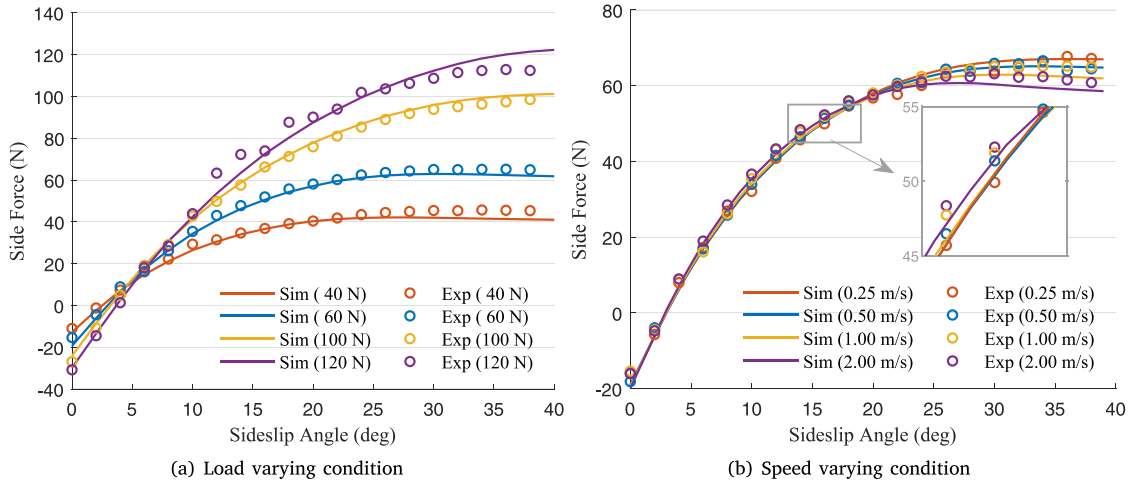


Fig. B.18. Results from model  $M_p$ .

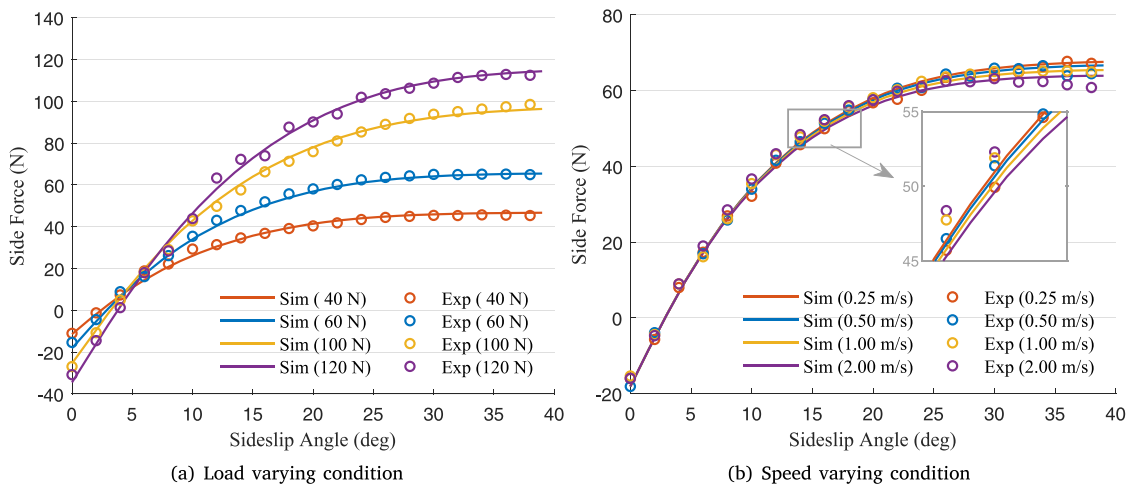


Fig. B.19. Results from model  $M_c$ .

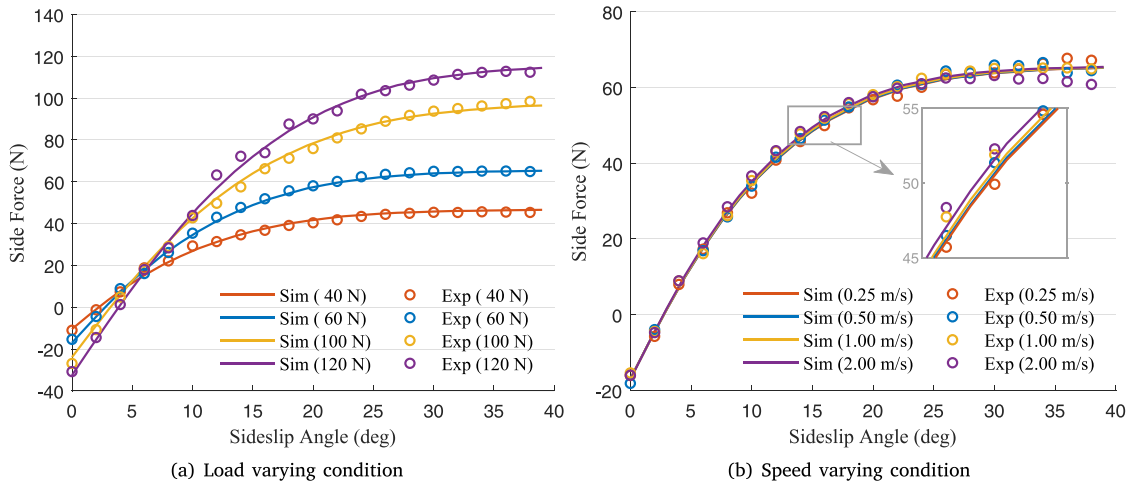


Fig. B.20. Results from model  $M_{\mu_1}$ .

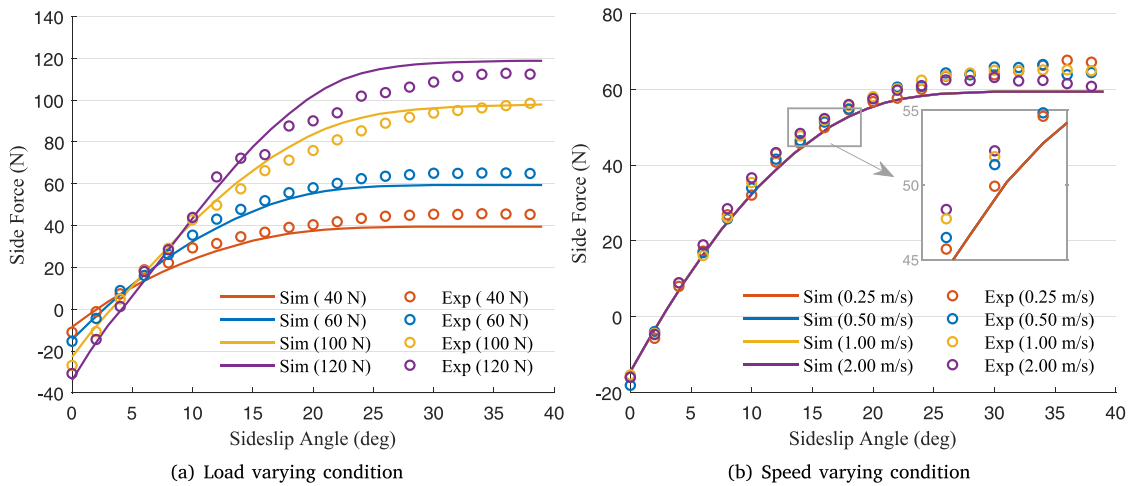


Fig. B.21. Results from model  $M_0$ .

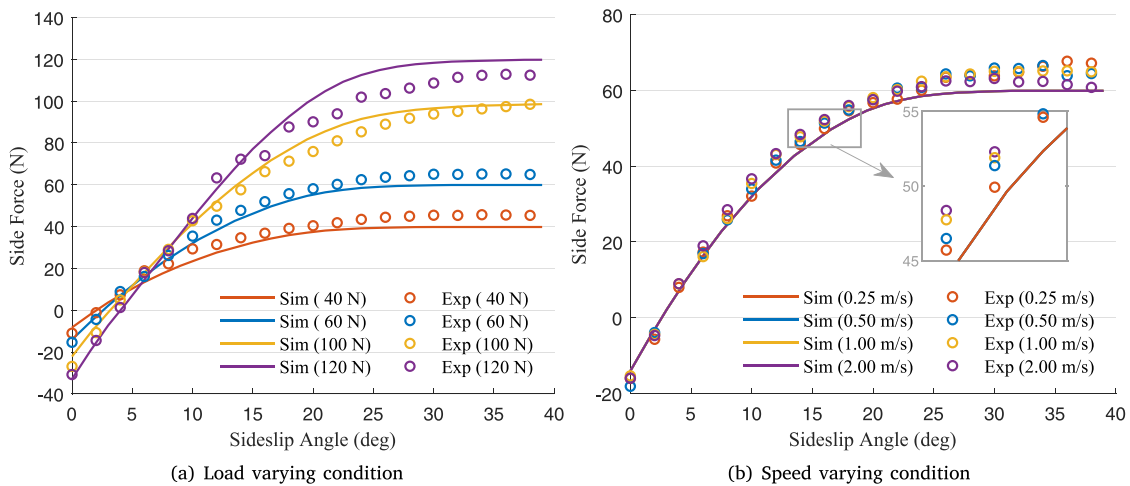


Fig. B.22. Results from model  $M_1$ .

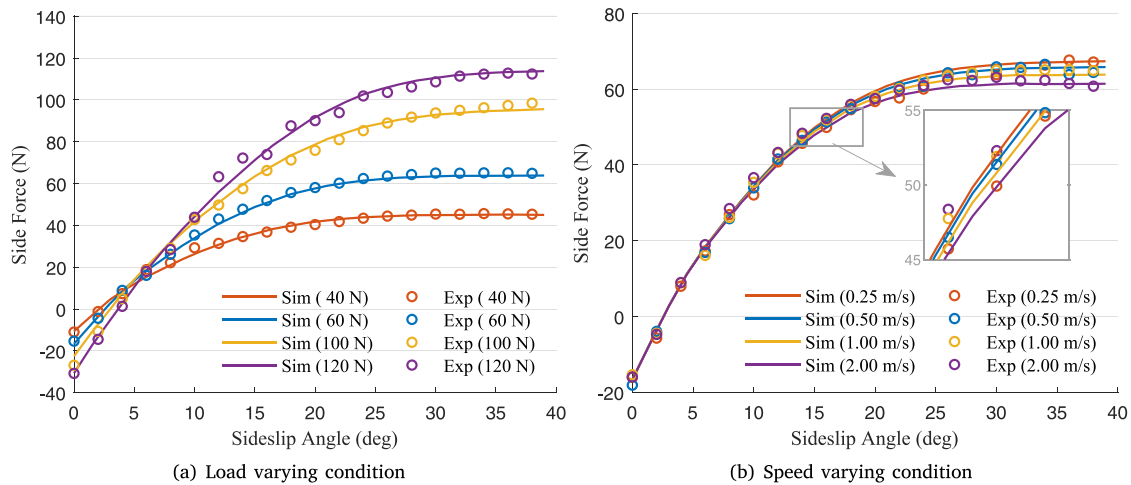


Fig. B.23. Results from model  $M_2$ .

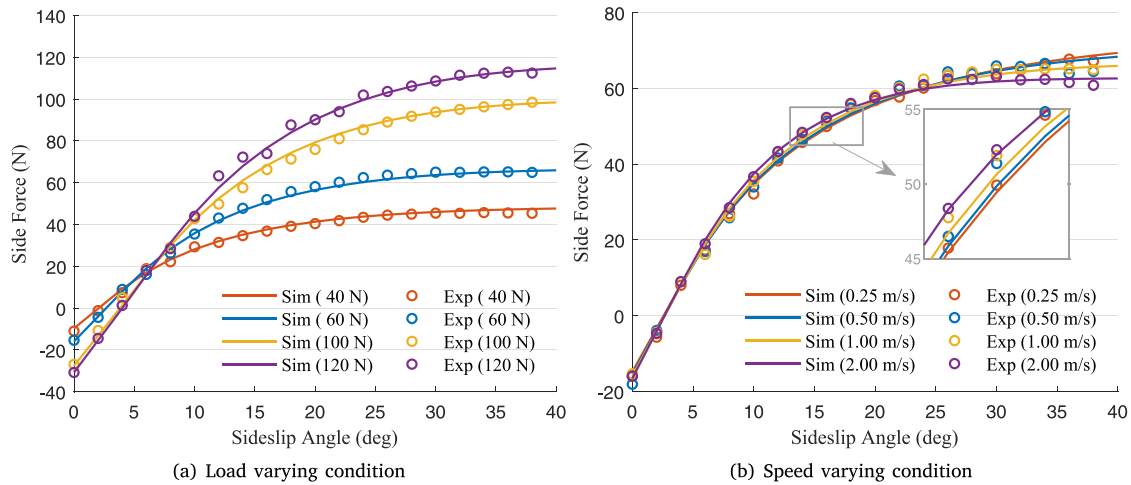


Fig. B.24. Results from model  $LuGre$ .

References

- [1] Bradley J, Allen R. Factors affecting the behaviour of rubber-tyred wheels on road surfaces. *Proc Inst Mech Eng* 1930;25(1):63–92.
- [2] Schlippe Bv, Dietrich R. Das Flattern eines bepannten Rades (Shimmying of a pneumatic wheel) *Bericht* 1941;140:35–45.
- [3] Fromm H. Kurzer Bericht über die geschichte der Theorie des Radflatterns. *Bericht* 1941;140:53.
- [4] Hadekel R. The mechanical characteristics of pneumatic tires. *Clearinghouse Fed Sci Tech Inf* 1952.
- [5] Dugoff H, Fancher PS, Segel L. Tire performance characteristics affecting vehicle response to steering and braking control inputs. Final report. Tech rep, Office of Vehicle Systems Research; 1969.
- [6] Gim G. Vehicle dynamic simulation with a comprehensive model for pneumatic tires [Ph.D. thesis], The University of Arizona; 1988.
- [7] Dahl PR. A solid friction model. *Aerosp Corp* 1968;18(1):1–24.
- [8] Dahl PR. Solid friction damping of mechanical vibrations. *AIAA J* 1976;14(12):1675–82.
- [9] De Wit CC, Olsson H, Astrom KJ, Lischinsky P. A new model for control of systems with friction. *IEEE Trans Autom Control* 1995;40(3):419–25.
- [10] Canudas-de Wit C. Comments on “A new model for control of systems with friction”. *IEEE Trans Automat Control* 1998;43(8):1189–90.
- [11] Canudas-de Wit C, Tsiotras P, Velenis E, Basset M, Gissinger G. Dynamic friction models for road/tire longitudinal interaction. *Veh Syst Dyn* 2003;39(3):189–226.
- [12] Deur J, Asgari J, Hrovat D. A 3D brush-type dynamic tire friction model. *Veh Syst Dyn* 2004;42(3):133–73.
- [13] Deur J, Kranjčević N, Hofmann O, Asgari J, Hrovat D. Analysis of lateral tyre friction dynamics. *Veh Syst Dyn* 2009;47(7):831–50.
- [14] Liang W, Medanic J, Ruhl R. Analytical dynamic tire model. *Veh Syst Dyn* 2008;46(3):197–227.
- [15] Li J, Zhang Y, Yi J. A hybrid physical-dynamic tire/road friction model. *J Dyn Syst Meas Control* 2013;135(1):0111007.
- [16] Mavros G. Tyre models for vehicle handling analysis under steady-state and transient manoeuvres [Ph.D. thesis], Loughborough University; 2005.
- [17] Simoni L, Beschi M, Visioli A, Åström KJ. Inclusion of the dwell time effect in the LuGre friction model. *Mechatronics* 2020;66:102345.
- [18] Hieu N, Chung P. Analysis of stability and stick-slip motion of a friction-induced vibrating system with dwell-time effect. *Int J Mech Sci* 2021;205:106605.
- [19] Shao R, Wahle M, Zimmermann M. A model for the dynamic friction behaviour of rubber-like materials. *Tribol Int* 2021;164:107220.
- [20] Sakai H. Theoretical and experimental studies on the dynamic properties of tyres part 1: Review of theories of rubber friction. *Int J Veh Des* 1981;2(1):78–110.
- [21] Sakai H. Theoretical and experimental studies on the dynamic properties of tyres. Part 2: Experimental investigation of rubber friction and deformation of a tyre. *Int J Veh Des* 1981;2(2):182–226.
- [22] Sakai H. Theoretical and experimental studies on the dynamic properties of tyres: Part 3: Calculation of the six components of force and moment of a tyre. *Int J Veh Des* 1981;2(3):335–72.
- [23] Sakai H. Theoretical and experimental studies on the dynamic properties of tyres. Part 4: investigations of the influences of running conditions by calculation and experiment. *Int J Veh Des* 1982;3(3):333–75.
- [24] Davari MM. Exploiting over-actuation to reduce tyre energy losses in vehicle manoeuvres [Ph.D. thesis], KTH Royal Institute of Technology; 2017.

- [25] Sarkisov P. Physical understanding of tire transient handling behavior [Ph.D. thesis], TU Dresden; 2019.
- [26] Riehm P, Unrau H-J, Gauterin F. A model based method to determine rubber friction data based on rubber sample measurements. *Tribol Int* 2018;127:37–46.
- [27] Riehm P, Unrau H-J, Gauterin F, Torbrügge S, Wies B. 3D brush model to predict longitudinal tyre characteristics. *Veh Syst Dyn* 2019;57(1):17–43.
- [28] Ammon D. Vehicle dynamics analysis tasks and related tyre simulation challenges. *Veh Syst Dyn* 2005;43(sup1):30–47.
- [29] Rauh J, Mössner-Beigel M. Tyre simulation challenges. *Veh Syst Dyn* 2008;46(S1):49–62.
- [30] Salehi M, Noordermeer JW, Reuvekamp LA, Blume A. Understanding test modalities of tire grip and laboratory-road correlations with modeling. *Tribol Lett* 2021;69(3):116.
- [31] Tuononen AJ. Digital image correlation to analyse stick–slip behaviour of tyre tread block. *Tribol Int* 2014;69:70–6.
- [32] Gnadler R, Fischlein H, Frey M, et al. Ermittlung von my-Schlupf-Kurven an PKW-Reifen. *FAT-Schriftenreihe* 1995;(119).
- [33] Svendenius J. Tire modeling and friction estimation [Ph.D. thesis], Lund University; 2007.
- [34] Goyal S. Planar sliding of a rigid body with dry friction: limit surfaces and dynamics of motion [Ph.D. thesis], Cornell University Ithaca, NY; 1989.
- [35] Lang A, Klüppel M. Influences of temperature and load on the dry friction behaviour of tire tread compounds in contact with rough granite. *Wear* 2017;380:15–25.
- [36] Kanafi MM, Tuononen AJ, Dorogin L, Persson BN. Rubber friction on 3D-printed randomly rough surfaces at low and high sliding speeds. *Wear* 2017;376:1200–6.
- [37] Grigoriadis K, Mavros G, Knowles J, Pezouvanis A. Experimental investigation of tyre–road friction considering topographical roughness variation and flash temperature. *Tribol Int* 2023;181:108294.
- [38] Schallamach A. The load dependence of rubber friction. *Proc Phys Soc Sect B* 1952;65(9):657.
- [39] Maegawa S, Itoigawa F, Nakamura T. Effect of normal load on friction coefficient for sliding contact between rough rubber surface and rigid smooth plane. *Tribol Int* 2015;92:335–43.
- [40] Guo K, Lu D. UniTire: unified tire model for vehicle dynamic simulation. *Veh Syst Dyn* 2007;45(S1):79–99.
- [41] Salehi M, Noordermeer JW, Reuvekamp LA, Tolpekina T, Blume A. A new horizon for evaluating tire grip within a laboratory environment. *Tribol Lett* 2020;68:1–18.
- [42] Romano L, Bruzelius F, Jacobson B. An extended LuGre-brush tyre model for large camber angles and turning speeds. *Veh Syst Dyn* 2023;61(6):1674–706.
- [43] Bruzelius F, Hjort M, Svendenius J. Validation of a basic combined-slip tyre model for use in friction estimation applications. *Proc Inst Mech Eng D* 2014;228(13):1622–9.
- [44] Svendenius J, Gäfvert M. A semi-empirical tyre model for combined slips including the effects of cambering. *Veh Syst Dyn* 2005;43(sup1):317–28.
- [45] Riehm P. Zur Wechselwirkung zwischen Fahrbahntextur und Laufstreifenmischung von Pkw-Reifen. *KIT Scientific Publishing*; 2023.
- [46] Yamashita H, Jayakumar P, Sugiyama H. Physics-based flexible tire model integrated with LuGre tire friction for transient braking and cornering analysis. *J Comput Nonlinear Dyn* 2016;11(3):031017.